Engineering Failure Analysis 146 (2023) 107112

Contents lists available at ScienceDirect

Engineering Failure Analysis

journal homepage: www.elsevier.com/locate/engfailanal

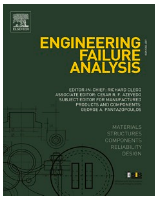

Investigating the impact of weld dilution and local mismatch on the low-cycle fatigue failure of Alloy 182 dissimilar weld transition under intermediate isothermal condition

Shutong Zhang [a], Sebastian Romo [a,b], Rafael A. Giorjao [a], Kaue C. Riffel [a,c], Antonio J. Ramirez [a,*]

[a] *The Ohio State University, Materials Science and Engineering Department, Columbus, OH, USA*
[b] *Institución Universitaria Pascual Bravo, Facultad de Ingeniería, Medellín, Colombia*
[c] *Federal University of Santa Catarina, Mechanical Engineering Department, Florianopolis, Brazil*

ARTICLE INFO

Keywords:
Electron microscopy
Low-cycle fatigue
Digital image correlation
Dissimilar joint
Cyclic plasticity

ABSTRACT

Dissimilar welded joints are the critical region that determines the operation lifetime of pressure vessels under severe cyclic deformation. The failure susceptibility of dissimilar welded joints is attributed to local strength mismatch and heterogeneous microstructures. This study evaluated the isothermal low-cycle fatigue performance of a dissimilar welded joint between nickel-based Alloy 182 and 1.25Cr-0.5Mo steel at 250 °C. During low-cycle fatigue tests, the Alloy 182 weld metal exhibited significant cyclic hardening over the 1.25Cr-0.5Mo steel base metal. The local strain variations in the weld transition were measured using the digital image correlation (DIC) technique to reveal the impact of material strength and hardening mismatch upon the cyclic behavior within the weld transition. Microhardness measurements of as-welded and cyclically deformed weld transition regions were performed to assess the hardening due to cyclic deformation. The WT failures occurred in the weld metal region adjacent to the fusion boundary. In addition, microstructural characterization shows that the crack initiation occurred within the weld dilution region, and the short crack growth was affected by microstructural heterogeneity in the weld metal.

1. Introduction

Coke drums are large pressure vessels used in oil-refining process to produce light-weight oil products and solid cokes through thermal cracking of heavy hydrocarbon molecules. Significant thermal variations during the heating and quenching of coke drums induce thermal stresses that cause damage in the vessels. Welding repairs with Ni-steel dissimilar welded joints have been widely used to restore the structural integrity of the damaged regions in coke drums. The Ni-base weld metal (WM) provides good strength, corrosion resistance, and weldability with the low-alloy steel (LAS). However, the dissimilar weld transition region is also susceptible to failure due to the inherent metallurgical defects, mechanical incompatibilities, and geometrical discontinuities [1].

Alloy 82 (ERNiCr-3) and Alloy 182 (ENiCrFe-3) are common Ni-base filler metals used for welding repairs of low-alloy steel (LAS) components. Hou et al. showed that Alloy 82/182 WM matches or slightly undermatches the LAS base metal [2]. However, the Ni-base

---

* Corresponding author.
E-mail address: ramirez.49@osu.edu (A.J. Ramirez).

https://doi.org/10.1016/j.engfailanal.2023.107112
Received 16 November 2022; Received in revised form 12 January 2023; Accepted 4 February 2023

WM significantly undermatches the LAS HAZ according to the microhardness indentation and miniature tensile tests [2–4]. As a result, the soft WM region undergo a large plastic strain due to the constraining effect of the hard HAZ region. According to Fan et al., the degree and range of the constraining effect is determined by the mismatch of yield strength and hardening between the hard and soft regions [5]. Therefore, the local strength mismatch has been identified as the major reason for the interface failure of dissimilar joints [6–8]. However, the impact of local mismatch on the strain distribution at the dissimilar weld interface has not been fully addressed. One of the major reasons is the lack of quantitative strain measurement of WT. In recent years, digital image correlation (DIC) analysis has been widely employed to evaluate the strain distribution within dissimilar joints [9–12]. Therefore, it is meaningful to use this approach to quantitively analyze the strain distribution in Alloy 82/182 dissimilar joints.

In addition to the local mismatch, the failure of Alloy 82/182 dissimilar joints is associated with metallurgical defects at the weld transition (WT) region, including weld dilution (WD) and heterogenous microstructure. WD affects the chemical composition and the microstructure heterogeneity at the dissimilar weld interface. One phenomenon is the carbon migration from the BM to the Ni-base alloy [1]. At the dissimilar weld interface, a soft ferrite layer forms at the carbon-depleted region, and a hard martensite layer forms at the partially mixed zone (PMZ) with a rich carbon diffusion and a steep compositional gradient [13]. The soft carbon-depleted region is susceptible to deformation due to the restraining effect from the adjacent hard microstructure [1], and the hard martensite layer is also detrimental as it promotes hydrogen-induced cracking at the weld interface [13–15]. Large welding heat input and dwell time at the elevated temperature promote the carbon migration at the weld interface [16]. In addition, WD increases the Fe contents in the Ni-base weld metal, lowering the solubility of other strengthening elements such as Mo, Nb, and Ti [17,18]. Sandhu and Shahi reported that the increasing weld dilution reduces the fatigue strength and resistance of Alloy 625 clad to 304L stainless steel [19].

Regarding the heterogeneous microstructure, Type I and Type II grain boundaries (GB) are typical features observed at the interface of Ni-LAS dissimilar joints. Type I GB forms during the columnar grain growth, which is perpendicular to the interface. Type-II grain boundary (GB) grows parallel to the weld interface of the Alloy 82/182-LAS dissimilar joints. Type-II GB is a high angle grain boundary (HAGB) that forms and propagates into the WM within the austenitizing temperature range [20,21]. Carbide formation at Type-II GB induces the GB embrittlement that causes the WM debonding and stress corrosion cracking (SCC) [22–24]. A composition gradient occurs within the range from the dissimilar weld interface to Type-II GB [21]. The range can be increased by the heat input and exhibits a higher hardness than the carbon-depleted region and the WM region beyond Type-II GB. Under deformation, Type I and Type II GBs become the preferential sites for crack nucleation and growth.

Compared with monotonic loading, cyclic loading during low-cycle fatigue (LCF) incurs more plastic strain accumulation in the Alloy 82/182-LAS dissimilar joints. In addition, cyclic behavior and strain distribution within different weld regions become more complicated considering the tension–compression loading [25]. However, few studies have been performed to evaluate the behavior and failure mechanism of Alloy 82/182-LAS dissimilar joints under cyclic loading. Therefore, it is meaningful to further evaluate the impact of local mismatch and weld defects on the LCF performance. In this study, an Alloy 182 dissimilar weld coupon was fabricated using the temper-bead welding (TBW) technique, widely adopted for welding repairs to temper HAZ microstructure in place of post-weld heat treatment [26–28]. Welding was implemented based on the standard welding repair procedure for coke drums. The BM, WM, and WT regions were evaluated using dog-bone shaped samples extracted from the weld coupon under strain-controlled ILCF tests. The temperature range for coke drums operation varies from 100 °C to 480 °C [29]. The most severe deformation in coke drums was reported to occur at 250 °C during the quenching stage [30]. Hence, the intermediate temperature 250 °C was selected as the isothermal condition for the ILCF tests and deformation was introduced by fully-reversed cyclic loading at ±0.01, ±0.015, and ±0.02 strain amplitudes. Metallurgical characterization of the WT region was performed in the as-received and cyclically deformed samples. Digital image correlation (DIC) analysis was employed to measure the local strain distribution within the WT region under cyclic deformation. In addition, failure analysis of WT samples was performed to elucidate the interfacial cracking susceptibility due to local strength mismatch and welding defect.

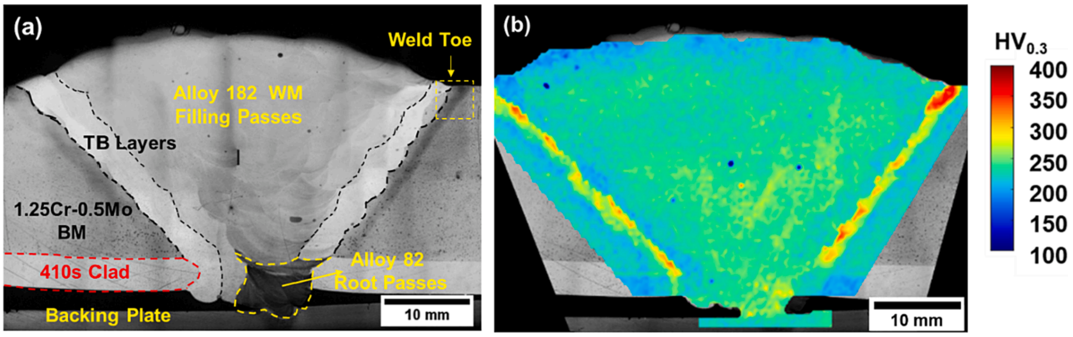

Fig. 1. (a) Macrograph of Alloy 82/182-1.25Cr-0.5Mo dissimilar weld transverse cross-section and (b) microhardness mapping.

2. Materials and method

2.1. Materials and welding parameters

According to Fig. 1(a), the welded joint was fabricated with a low-alloy steel BM plate clad with 410 s ferritic stainless steel and Alloy 82/182 weld metal. The BM plate possesses a nominal alloying composition of 1.25Cr-0.5Mo, which belongs to the ASME SA 387 Grade 11 Class 2 steel. The BM was normalized 940 °C for 40 min and tempered at 720 °C for 15 min. The root passes of the coupon were welded with Alloy 82 filler metal using the gas tungsten arc welding (GTAW) process and the temper bead (TB) layers and filling passes were welded with Alloy 182 filler metal using the shield metal arc welding (SMAW) process. The welded joint is a double V-groove shape design with a 50° bevel angle on each side. The welding parameters are presented in Table 1. The TB layers consisted of two layers welded with a lower heat input than the filling passes to restrict the size of HAZ. The high-hardness microstructure created by the 1st layer of TB welding was tempered by the second layer of TB welding. Therefore, TB welding serves as a similar function as PWHT in terms of tempering hard microstructures, and the process is commonly implemented when PWHT is not practical [31]. According to Fig. 1(a), the TB layers exhibit a lighter etch than the Alloy 182 filling passes. The chemical compositions of the BM and WM filling passes measured using an optical spectrometer (OS) is shown in Table 2. Root passes welded with Alloy 82 are not considered in this study, as the samples were extracted within the filling passes region welded with Alloy 182.

2.2. Sample extraction and isothermal low-cycle fatigue test

As is shown in Fig. 2 (a) and (b), fatigue samples were extracted transverse to the welding direction and the sample gauge sections were in the WM, BM, and WT regions of the welded joint. The sample gauge section is a rectangular shape with 6 mm × 6 mm cross-section and 10 mm-distance width. The transition radius from the reduced gauge section to the holding section is 6.35 mm. Prior to the ILCF tests, the sample surface was grinded with 240, 400, 600, 800, and 1200 mesh-size SiC paper and the sample edges were rounded using 240 mesh-size SiC paper to minimize stress concentration due to the sample geometry.

Strain-controlled ILCF tests were performed using the Gleeble® 3800 thermo-mechanical simulator at 250 °C. The ILCF tests were performed at ± 0.01, ± 0.015, and ± 0.02 strain amplitudes with 0.002/s strain rate under the 250 °C isothermal condition. The bulk strain of gauge section was measured and controlled using the Epsilon™ high-temperature axial extensometer. A triangular wave signal was applied to perform the fully-reversed cyclic loading. Sample heating was performed using the resistance heating process and controlled by a K-type thermocouple welded at the center of gauge section.

2.3. Digital image correlation analysis of WT sample under cyclic deformation

As is shown in Fig. 3, DIC analysis was performed to measure the local surface strain of the WT sample using a Sony® digital camera with a high-resolution lens. The two-side measurements from the strain gauge and the digital camera were correlated to each other because the through-thickness variation was assumed to be negligible in the WT sample. DIC local strain measurement was performed at ± 0.01, ± 0.015, and ± 0.02 strain amplitudes. A fatigue sample was pre-loaded with 15 cycles at ± 0.01 strain amplitude and then tested for 10 cycles at a sequence of ± 0.01, ± 0.015, and ± 0.02 strain amplitudes respectively with a 0.002/s strain rate. The first 15 cycles of pre-loading enabled the fatigue sample to reach its saturated stress condition, so the cyclic stress quickly stabilized when switching to a higher strain amplitude. The temperature of the sample gauge section was controlled at 250 °C. DIC strain analysis was performed using the VIC-2D system to calculate the von-mises effective strain (ε_ν) of the WT, which is defined as

$$\varepsilon_\nu = \frac{2}{3}\sqrt{\varepsilon_1^2 - \varepsilon_1\varepsilon_2 + \varepsilon_2^2}, \tag{1}$$

where ε_1 and ε_2 are the major and minor principal strain values.

$$\varepsilon_1, \varepsilon_2 = \frac{\varepsilon_{xx} + \varepsilon_{yy}}{2} \pm \sqrt{\left(\frac{\varepsilon_{xx} - \varepsilon_{yy}}{2}\right)^2 + \left(\frac{\gamma_{xy}}{2}\right)^2}, \tag{2}$$

2.4. Metallurgical characterization and failure analysis

The microstructure at the weld transition region was characterized using optical microscope (OM) and scanning electron microscope (SEM). Samples were sectioned from the cross-section of the welded joint, and grinded with SiC paper with a mesh-size sequence

Table 1
Summary of welding parameters.

Welding Passes	Materials	Process	Preheat/Interpass Temperature (°C)	Travel Speed (mm/s)	Current (A)	Voltage (V)	Heat Input (J/mm)
Root Pass	Alloy 82	GTAW	197	1.3	126	11	1091
TB Layer	Alloy 182	SMAW	203	2.4	81	25	854
Filling Pass	Alloy 182	SMAW	212	2.3	95	25	1039

Table 2
Chemical composition of BM and WM (wt.%) measured by optical spectroscopy.

	C	Mn	P	S	Si	Mo	Cr	Ni	Cu	Nb	Ti	Fe
1.25Cr-0.5Mo	0.13	0.61	0.01	0.01	0.55	0.6	1.5	0.18	0.11	0.00	0.01	Bal.
Alloy 182	0.06	7.13	0.02	0.01	0.49	0.11	15.45	Bal.	0.02	1.85	0.11	9.91

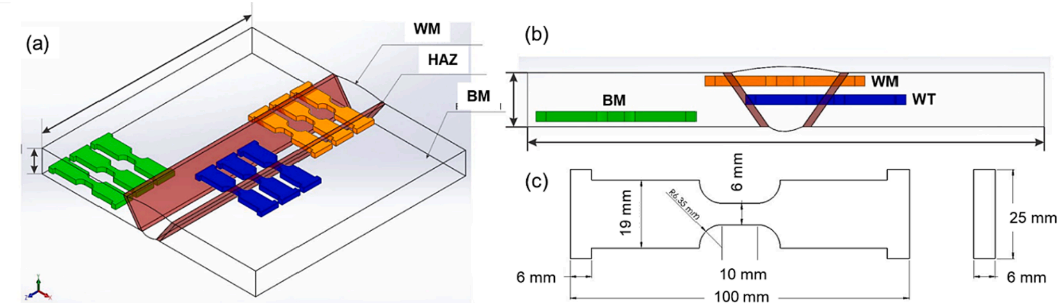

Fig. 2. Schematic of fatigue samples position and design. (a) Isometric project of sample positions within the welded joint. (b) Sample positions at the transverse cross-section. (c) Dog-bone sample design.

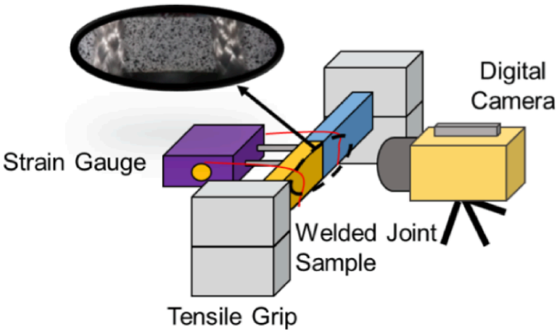

Fig. 3. Schematic of a double-side strain measurement set-up. The strain gauge is used for bulk strain measurement and strain control. Digital camera is used for local strain measurement.

of 200, 400, 600, 800, and 1200. Then the samples were polished using 6 μm and 1 μm diamond paste and finished with 0.02 μm colloidal silica vibratory polishing. Metallography samples at WT were prepared using a 2.0 % Nital etchant (2.0 % Nitric acid and 98 % ethanol) and 10 % chromic acid (10 wt% Cr_2O_3 and 90 ml distilled water) electrolytic etching under 2.5 Volts for 1 min. Compositional gradient in the WT region and solute element segregation in the solidification microstructure were investigated using energy-dispersive spectroscopy (EDS).

Vickers microhardness measurements were performed in the cross-section shown in Fig. 1 (b) and in the as-welded WT and the WTs of fatigue samples tested at ±0.01, ±0.015, and ±0.020 strain amplitudes. Automatic indentation and microhardness measurement were implemented using a LECO LM100AT microhardness system with a load of 300 g. The microhardness mapping of the weld cross-section was constructed by an indentation matrix with 500 μm inter-space in x and y directions. The WT regions was analyzed with an indentation matrix with 150 μm inter-space in x and y directions.

Electron microscopy analysis of weld microstructure and fracture surface was performed using a FEI APREO SEM. The chemical composition profile at the vicinity of weld interface was measured using EDS line analysis. To identify the crack initiation location, EDS point analysis was implemented at the fracture surface of a WT sample. The 3D topography of a WT fracture surface was obtained using an Olympus DSX 510 digital microscope with an extended focal image function. In addition, the as-received and after-fatigue weld interfaces were characterized using electron backscattered diffraction (EBSD) technique. The operation voltage and beam current used for analysis were 10 kV and 6.4nA. The EBSD scanning step size was 0.2 μm. EBSD data was analyzed using the OIM software to generate the inverse pole figure (IPF), phase ID mapping, and kernel average misorientation (KAM) map of the scanning regions.

3. Results

3.1. Metallurgical characterization

Fig. 1 (b) shows the microhardness mapping of the weld cross-section. The TBW was effective in tempering most of the HAZ microstructure as evidenced by the lower hardness observed in comparison with the single-bead HAZ region at the weld toe. Nevertheless, the process did not fully temper the HAZ microstructure, as some high-hardness regions are still detected in the mapping. The filling passes exhibit homogeneous hardness, matching the hardness at the BM region. A local soft region was found in the TB layers, which are overmatched by the neighboring HAZ and the region of filling passes. Fig. 4(a) reveals the microstructure configuration within the WT region, and Fig. 4 (b)–(i) show the microstructure in the different WT regions. The unaffected BM exhibits a tempered bainitic microstructure. The IC-HAZ exhibits a mixture of tempered bainite and martensite due to the temperature range between the lower and upper critical temperatures (A_1 and A_3). The CG-HAZ exhibits a mixture of tempered and not fully tempered martensite. The FG-HAZ shows fine martensite and granular bainite. The WT interface in Fig. 4 (f) shows a featureless planar growth zone next to the fusion boundary and an epitaxial columnar growth region. The etching contrast between the 1st and the 2nd WM layer indicates the difference in WD. The buttering layer possesses a larger portion of Fe content from the BM than the rest of the WM and exhibits a lightly etched columnar microstructure compared with the subsequent layers with less dilution. Fig. 5 (a)–(d) exhibit the EBSD analysis at the weld interface. A thin martensitic layer is observed along the fusion boundary due to the carbon migration from the neighboring BM [13]. Type-II GB was observed to form parallel to the fusion boundary, and a precipitation-free zone formed within the Type-II grains. The HAZ region exhibits a fine martensite-lath structure with a large amount of misorientation, as is shown in Fig. 5 (d).

Fig. 6 (a) reveals the variation of Fe, Ni, Cr, and Mn contents across the weld interface. A martensitic layer forms adjacent to the FB,

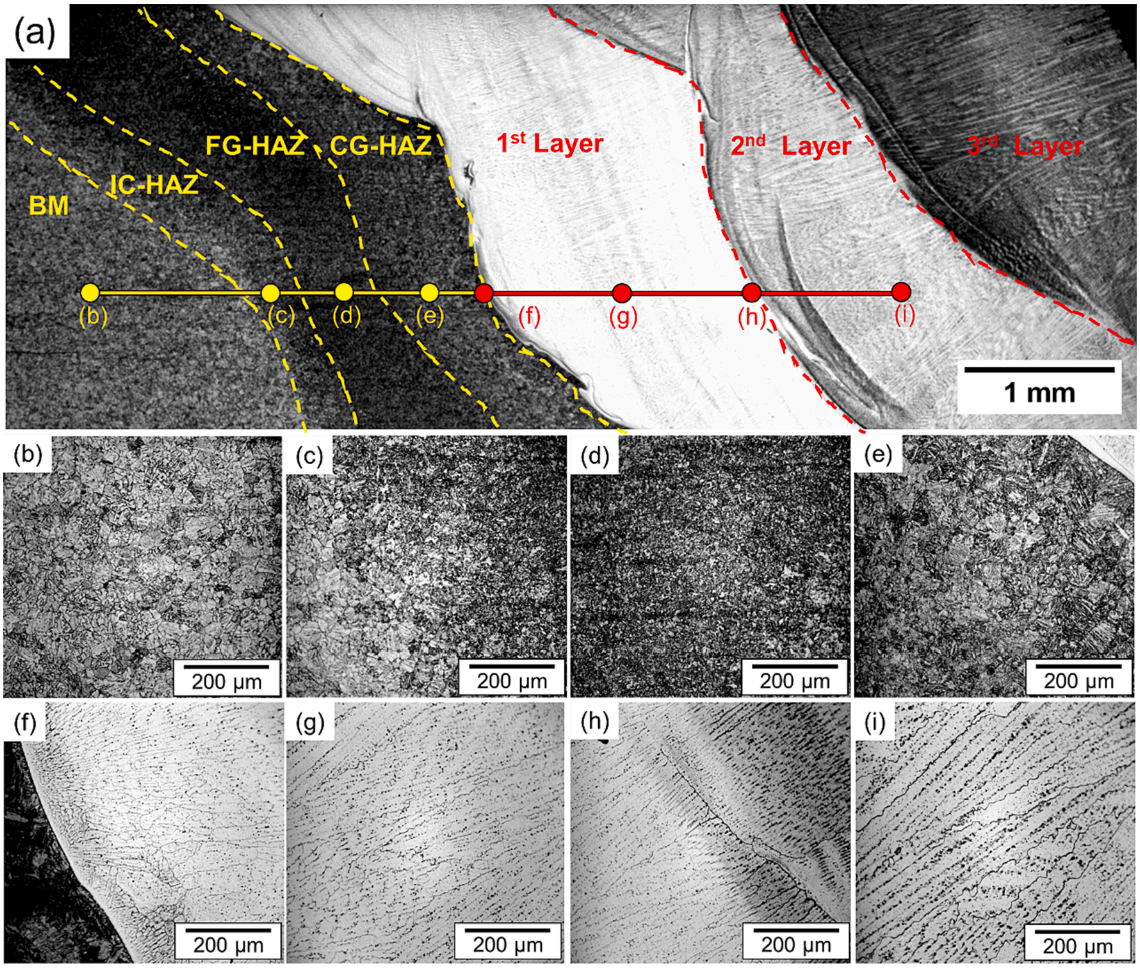

Fig. 4. As-welded Alloy 182-1.25Cr-0.5Mo WT microstructure under OM. (a) Microstructural configuration and different regions within the WT. OM microstructural images in (b) base metal, (c) IC-HAZ, (d) FG-HAZ, (e) CG-HAZ, (f) fusion boundary interface, (g) WM 1st layer, (h) 1st to 2nd WM layer interface, and (d) 2nd WM layer.

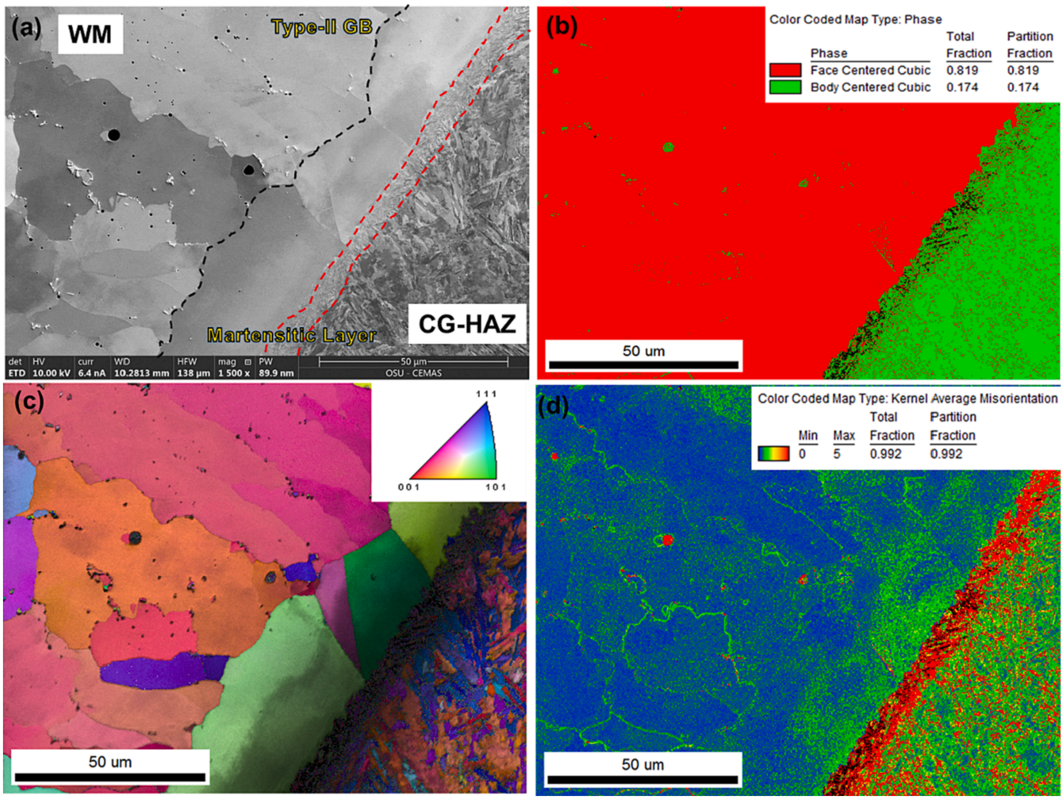

Fig. 5. EBSD analysis of the as-welded WT region. (a) Secondary image of the WT region. (b) BCC-FCC phase distribution. (c) IPF and IQ maps. (d) KAM map.

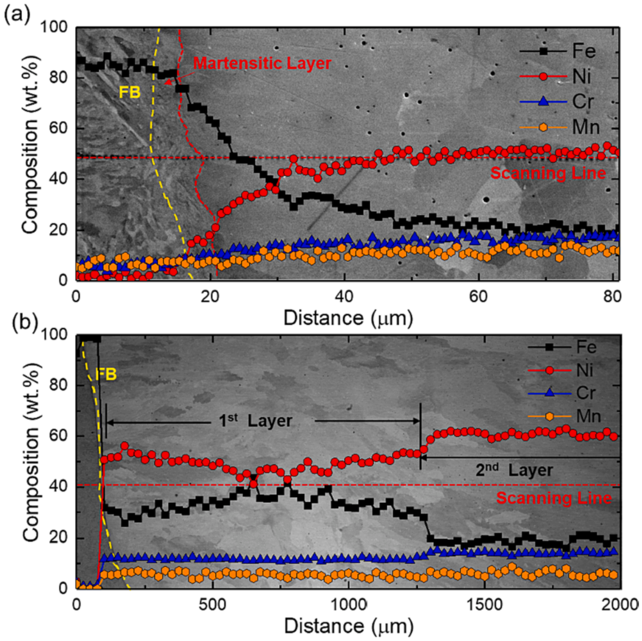

Fig. 6. Chemical composition variations across (a) the weld interface and (b) the weld metal layers close to the fusion boundary.

where the Fe content is above 80 %. A compositional gradient occurs within 40 μm from the FB. Fig. 6 (b) shows the compositional variation across the 1st and the 2nd WM layer. The contents of Cr and Mn exhibit little variation from the fusion boundary to the WM, whereas a stepwise transition of Fe and Ni contents is observed at the interface between the 1st and the 2nd WM layer. In contrast with the stable compositions in the 2nd layer, the compositions in the 1st WM layer exhibits unstable variations, indicating the uneven mixing of BM during the welding process. Using the Fe content in the 1st WM layer and the 2nd WM layer, the WD ratio were calculated based on the equation below:

$$WD = \frac{W_m^{Fe} - W_{WM}^{Fe}}{W_{BM}^{Fe} - W_{WM}^{Fe}}, \tag{3}$$

where W_m^{Fe}, $W_{\mathrm{WM}}^{\mathrm{Fe}}$ and $W_{\mathrm{BM}}^{\mathrm{Fe}}$ refer to the Fe content in the measured region, BM, and WM filling passes. The compositions of BM and WM filling passes were from Table 2. Therefore, the weld dilution in the 1st WM layer and the 2nd WM layer were estimated to be 27 % and 11 %, respectively.

Fig. 7 shows the backscattered electron (BSE) image and the EDS mapping of precipitates observed at the solidification grain boundary (SGB). According to the EDS mapping, the spherical-shaped black particle is a titanium oxide inclusion, and the irregular-shape bright particle attached to the SGB is a niobium carbide precipitate. Titanium oxide inclusions are dispersed in the dendritic regions and along the SGBs, while niobium carbide precipitates are mainly observed along the SGBs and solidification sub-grain boundaries (SSGBs). Fig. 8 (a)–(d) reveal the interdendritic precipitation and segregation in the 1st and 2nd WM layers. According to Fig. 8 (a) and (c), the 1st WM layer exhibits more precipitations than the 2nd WM layer. Niobium carbide precipitates are primarily located at the SGBs and SSGBs, while Titanium oxide inclusions are dispersed randomly in columnar grains and along GBs. The increasing Fe content due to the WM dilution is considered the primary cause for the larger number of precipitates in the 1st WM layer. Banovic et al. reported that the increasing Fe content controlled by WD promotes the Nb segregation at the interdendritic regions in nickel-base weld metals [17]. In addition, the carbon migration through the 1st WM layer further enhances the Nb-rich carbides precipitation. Fig. 8 (b) and (d) show the solute element segregation at the interdendritic regions. The 2nd WM layer exhibits a more significant Mn segregation than the 2nd WM layer, which explains the difference in the interdendritic regions in Fig. 4 (g) and (i). The Fe content decreases in the interdendritic regions, but the Cr content exhibits less variation in the interdendritic regions.

3.2. Isothermal low-cycle fatigue test

According to the monotonic stress–strain curves in Fig. 9, the BM is undermatched by the Alloy 182 WM in terms of yield strength and the WT exhibits a medium yield strength between WM and BM. Fig. 10 (a), (c), (e) show the cyclic response of half stress range ($\Delta\sigma/2$) over the normalized cycle (N/N_{80}) at ±0.01, ±0.015, and ±0.02 strain amplitudes. The yield strength at 250 °C of the 1.25Cr-0.5Mo BM and Alloy 182 WM are 462 MPa and 360 MPa based on 0.002 strain offset of the monotonic stress–strain data. Hence the BM is significantly under-matched by the WM during the first few cycles of loading. However, the cyclic stress of the WM quickly surpasses the cyclic stress of the BM due to the significant cyclic hardening. The WT sample exhibits a more rapid stress increase than the WM sample in the first few cycles and softens until failure. The cyclic stress range of WT lies between the stress range of the WM and the BM, as is shown in Fig. 10 (b), (d), (f). On the other hand, the stress–strain curves of WT show more similarity to the WM than the BM, indicating that the WM plays a more critical role than the BM in determining the cyclic behavior of the WT. It is noteworthy that the cyclic behavior of HAZ, which affects the behavior of WT, cannot be revealed from the bulk strain measurement. The fatigue life (N_{80}) is defined by the cycle when the half stress range drops by 20 % of the stabilized stress. According to the fatigue life results in Table 3, the BM fatigue life cycles show good agreement at each strain amplitude. In contrast, the WM fatigue life exhibits significant variation up to 87 % at 0.02 strain, which could be attributed to the heterogeneous weld microstructure as well as weld impurities and defects. In

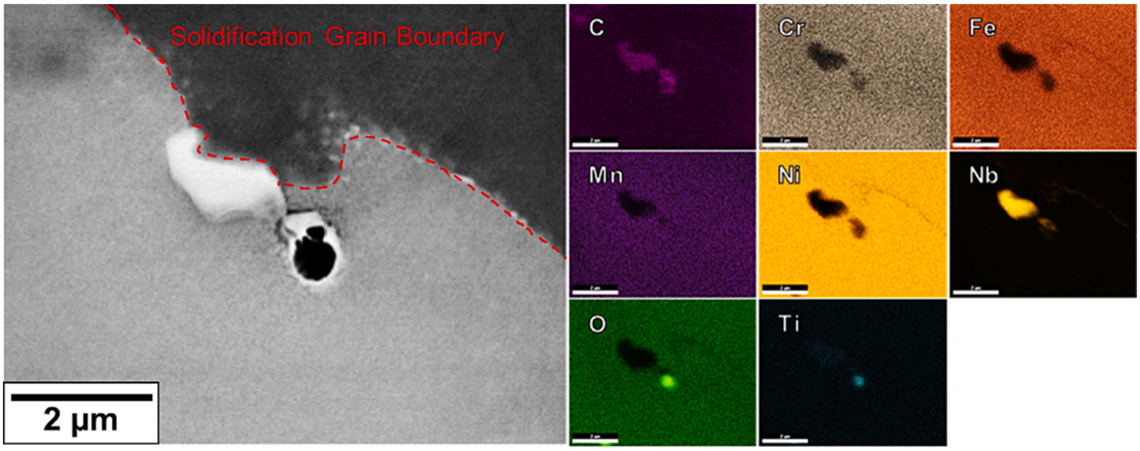

Fig. 7. Backscattered Electron (BSE) and EDS mapping of precipitates along the solidification grain boundary [32].

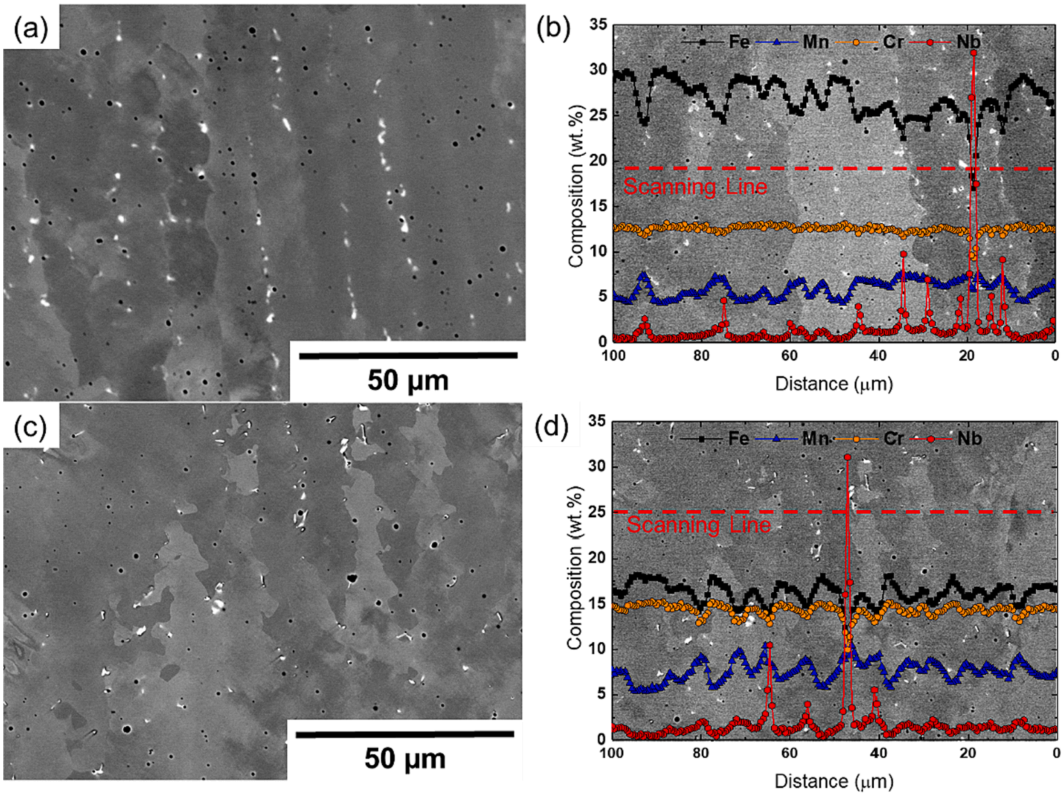

Fig. 8. Evaluation of solute element segregation and precipitation at the interdendritic regions. (a) BSE image and (b) EDS line analysis in the 1st WM layer. (c) BSE image and (d) EDS line analysis in the 2nd WM layer. The scanning line marked by the red dashed line is transverse to the columnar growth direction.

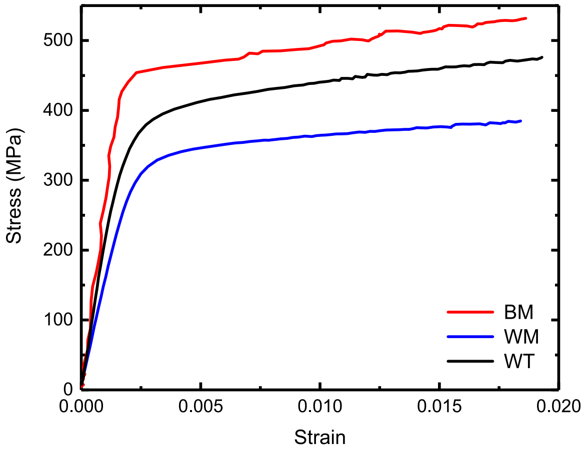

Fig. 9. Monotonic stress–strain curves of BM, WM, and WT samples at 250 °C.

general, the 1.25Cr-0.5Mo BM exhibits better fatigue resistance than the Alloy 182 WM, but both materials exhibit a significant life decrease with strain amplitudes. The WT region shows the lowest fatigue resistance compared with the BM and the WM, but the WT life cycles indicate a subtle decline with the strain amplitudes. The DIC measurement is presented to examine the local strain variation within the WT under cyclic deformation at 0.01, 0.015, and 0.02 strain amplitudes.

3.3. Digital image correlation analysis of weld transition

Fig. 11 (a)–(i) show the DIC analysis of the WT under cyclic loading at ±0.01, ±0.015, and ±0.02 strain amplitudes. Strain

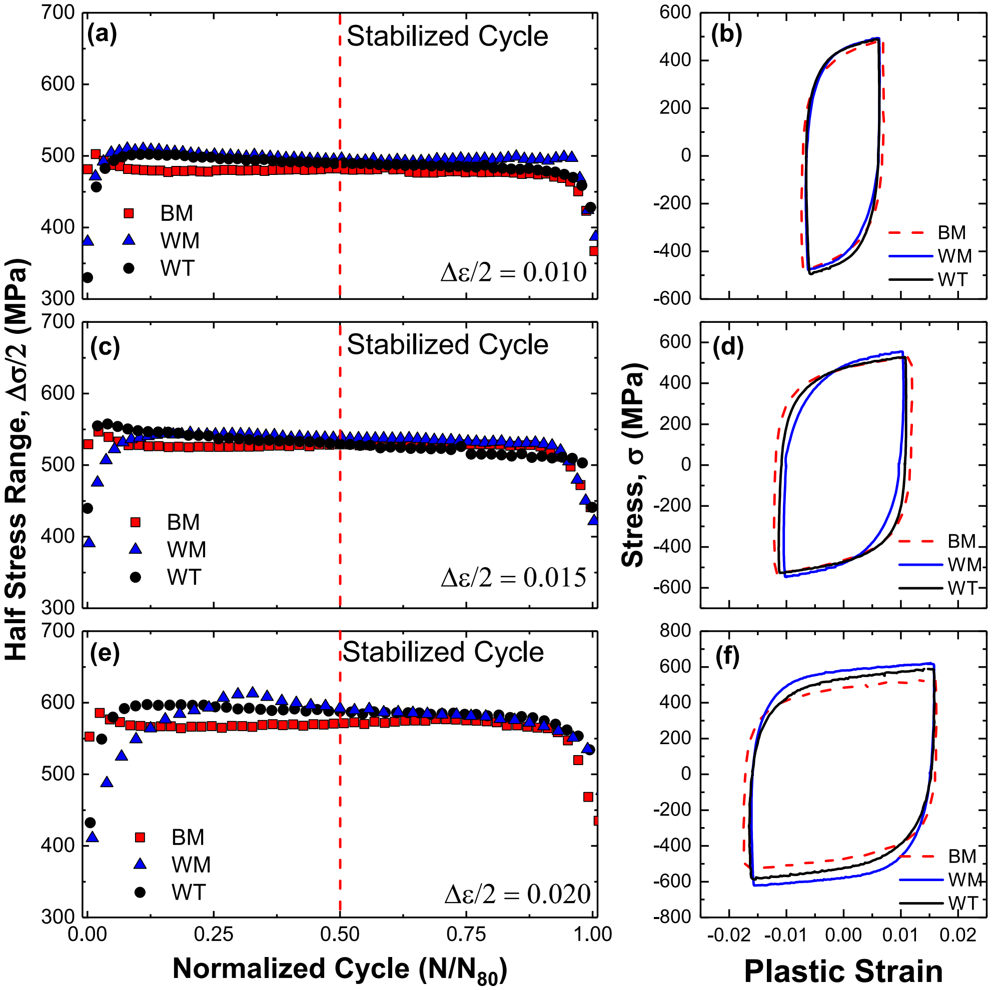

Fig. 10. Cyclic half stress range responses over normalized cycle (N/N_{80}) of BM, WM, and WT at (a) ±0.01, (c) ±0.015, and (e) ±0.02 strain amplitudes. Stabilized stress–strain curves comparison at (a) ±0.01, (c) ±0.015, and (e) ±0.02 strain amplitudes. The stabilized cycle refers to the half-life cycle (0.5 N_{80}).

Table 3

Summary of fatigue life (N_{80}) of BM, WM, and WT at different strain amplitudes.

ILCF Test (T = 250 °C)	$\Delta\varepsilon/2 = \pm0.01$		$\Delta\varepsilon/2 = \pm0.015$		$\Delta\varepsilon/2 = \pm0.02$	
	Test 1	Test 2	Test 1	Test 2	Test 1	Test 2
1.25Cr-0.5Mo	1570	1439	553	450	248	292
Alloy 182	634	911	296	253	193	103
Alloy 182-1.25Cr-0.5Mo WT	286	208	200	166	178	182

measurements at R_0, R_1, R_2, and R_3 reveal the average local strain variations of the 2nd WM layer, the 1st WM layer, the HAZ, and the BM, as is shown in Fig. 11 (a). Fig. 11 (b) and (c) show the axial strain (ε_{xx}) and von mises strain (ε_{von}) within the WT under tensile loading. The axial strain distributions reveal that the WM region (R_0, R_1) was under heavier deformation than the BM region (R_2, R_3) under tension. The local strain variations of each cycle were stable at ±0.01 and ±0.015 strain, as is shown in Fig. 11 (d)–(g). Local axial strains at R_0 and R_1 were relatively consistent, indicating that the impact of WD on the local strain distribution is not significant. The local mismatch of yield strength and hardening behavior within the WT leads to an asymmetrical cyclic strain in the WM and BM, although the bulk strain is fully reversed. Fig. 11 (d) and (f) show a positive mean axial strain in the 2nd WM layer (R_0) and the 1st WM layer (R_1) and a negative mean axial strain in the BM (R_3). In contrast, the cyclic strain at HAZ (R_2) is symmetrical, indicating the region is not affected by the mismatch. Fig. 11 (e) and (g) show a higher von mises strain at R_1 than R_0 during compression, as the HAZ constraining effect increases the shear strain at R_1. According to the von mises strain variation, the 1st and 2nd WM layers experienced the largest deformation during tension, while the BM received the largest deformation during compression. Compared with the local

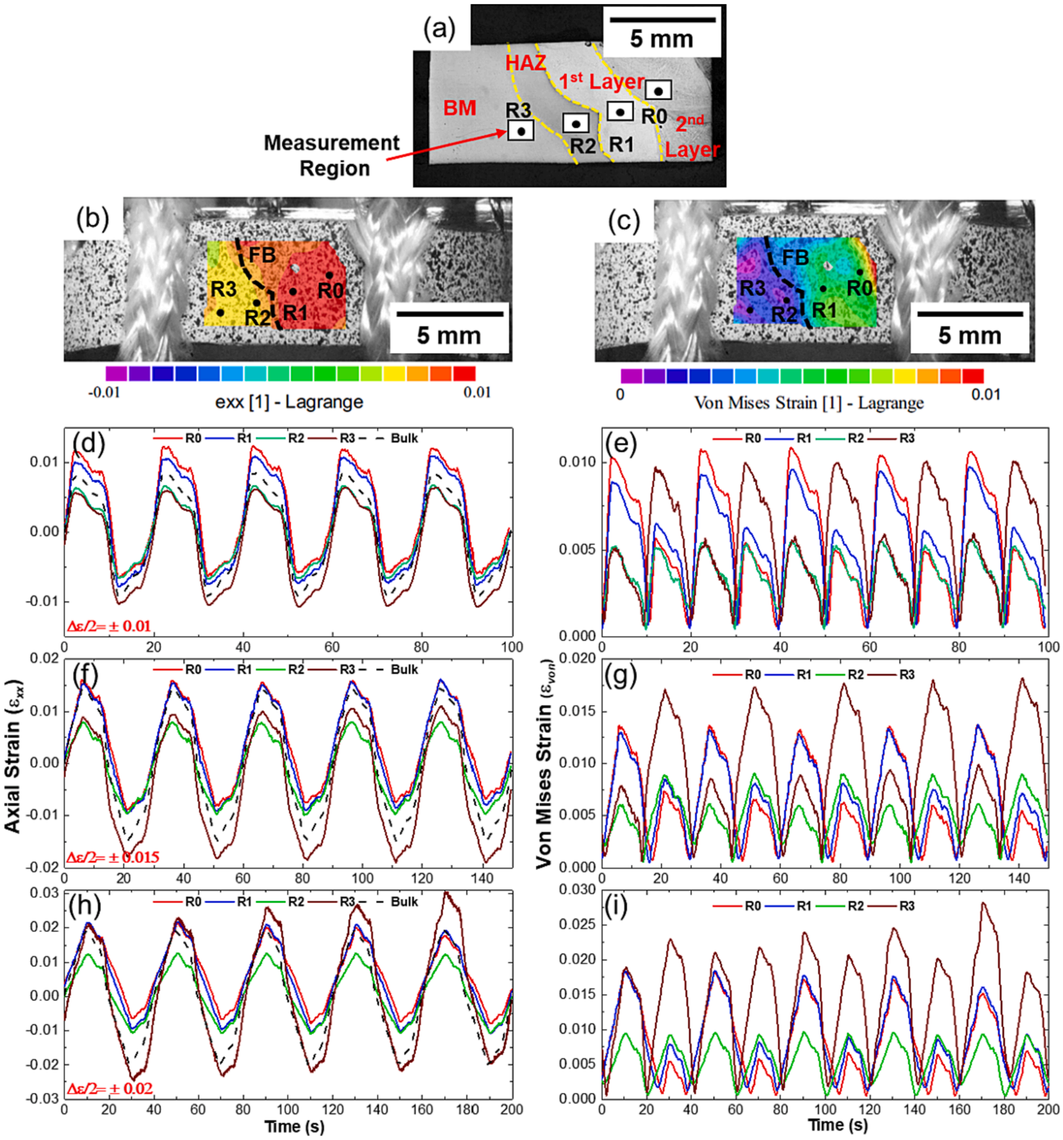

Fig. 11. DIC local strain analysis of WT stabilized cycles at ±0.01, ±0.015, and ±0.020 strain amplitudes. (a) Macrograph of WT and measurement locations. Point R_0, R_1, R_2, and R_3 represent the centers of measurement regions in the 1st WM layer, the 2nd WM layer, HAZ, and BM, respectively. (b) Axial strain (ε_{xx}) distribution and (c) Von Mises strain (ε_{von}) distribution within the WT. (d)(e) Axial and Von Mises strain variations of R_0, R_1, R_2, and R_3 at ±0.01 strain. (f)(g) Axial and Von Mises strain variations of R_0, R_1, R_2, and R_3 at ±0.015 strain. (h)(i) Axial and Von Mises strain variations of R_0, R_1, R_2, and R_3 at ±0.020 strain. Bulk strain in black dashed lines refers to the extensometer measurement.

strain measurements at ±0.01 and ±0.015 strain, the local strain measurement at ±0.02 strain exhibits the ratchetting phenomenon, especially in the BM. Interestingly, the BM mean strain moved towards the positive direction, while the mean strain of the WM 1st and 2nd WM layers moved towards the negative direction. As is shown in Fig. 11 (i), the BM region received the most significant deformation under both tensile and compressive loadings.

3.4. Failure analysis

3.4.1. Microhardness measurement

Fig. 12 (a)–(c) show the microhardness measurements and the etched macrographs of the WTs in the as-welded, 0.01, 0.015, and 0.02 strain fatigue samples. Based on the contrast difference of the WT macrographs, the region-distinction lines were drawn at the HAZ-BM border, FB, and inter-pass boundary between the 1st and the 2nd WM layer. The microhardness measurements reveal the local strength mismatch within the WT and the hardening effect caused by cyclic deformation. The microhardness of as-welded WT in Fig. 12 (a) shows that the WM and the BM possess similar hardness, which is lower than the HAZ hardness. The microhardness

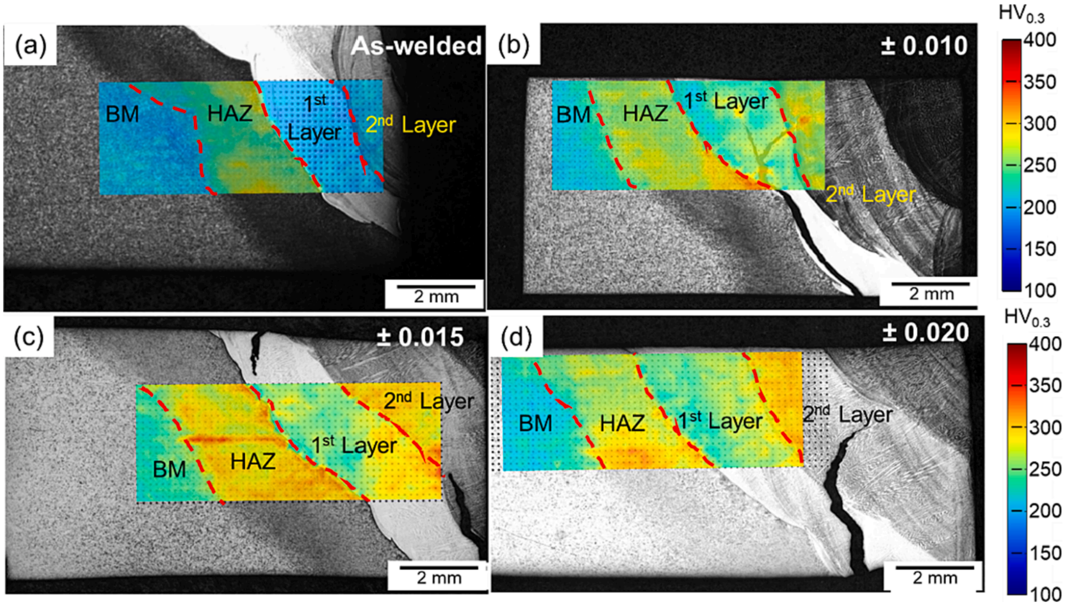

Fig. 12. Microhardness mapping of (a) As-welded WT, (b) fatigue WT tested at 0.01 strain amplitude, (c) fatigue WT tested at 0.015 strain amplitude, and (d) fatigue WT tested at 0.02 strain amplitude. The BM, HAZ and WM 1st and 2nd layers were identified based on the WT macrographs.

comparison indicates that local strength mismatches occur between WM and HAZ and between HAZ and BM.

Based on the results in Fig. 12 (a)–(d), the microhardness of all the WT regions increases with strain amplitudes from the as-welded condition to 0.015 and 0.02 strain amplitudes. However, further hardness increases are not observed from the 0.015 strain amplitude to the 0.02 strain amplitude. According to the average hardness variation in Fig. 13, the BM, HAZ, and the 1st WM layer exhibit a higher hardness at the 0.015 strain amplitude than at the 0.02 strain amplitude. Due to the unevenness of HAZ tempering and variation of sample extraction, the unexpected hardness change is likely induced by the pre-existing untempered HAZ in the 0.015 strain fatigue sample that enhances the cyclic hardening in the adjacent BM and the 1st WM layer. In terms of the hardness differences within the WT, the as-welded BM and the second WM layer exhibit similar microhardness, higher than the 1st WM layer but lower than the HAZ under the as-received condition. The hardness mismatch between the second WM layer and the 1st WM layer further increases in the fatigue WT samples, while the mismatch between the HAZ and the 1st WM layer is reduced after cyclic deformation. Nevertheless, the 1st WM layer adjacent to the weld interface is a consistently a local soft region, where the main cracks occur.

In addition to the microhardness distribution, Fig. 12 (b)–(d) also show the fatigue cracks initiate in the 1st WM layer and propagates parallel to the FB. The main cracks grow approximately 45° with respect to the loading direction; therefore, the growth is consistent with the expected direction of maximum shear stress at the macro-level. Fig. 12 (b) shows that the fatigue crack growth is deflected at the FB and then bifurcated into two cracks, one along the primary crack direction and the other along the solidification direction. The transverse cross-section in Fig. 12 (c) shows one crack in the 1st WM layer and another crack along the interpass boundary of the 1st WM layer and the 2nd WM layer. The interpass crack is associated with the mismatch between the 1st WM layer and the 2nd WM. On the cross-section of the 0.02 strain WT sample, the main crack in Fig. 12 (d) is observed to initiate in the 1st WM

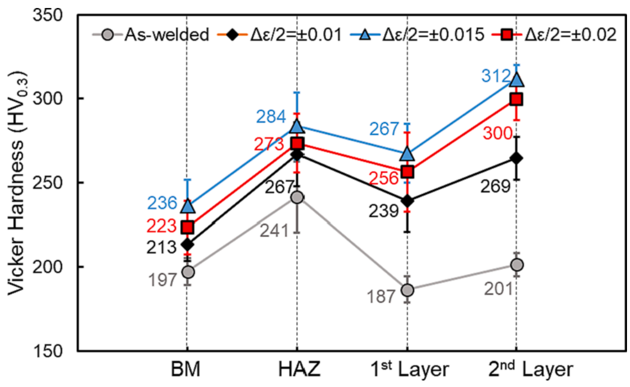

Fig. 13. Average microhardness variation within as-welded and cyclically deformed WTs.

layer and propagate into the 2nd WM layer along the solidification direction.

3.4.2. EBSD analysis of secondary crack

Fig. 14 (a)–(d) show the EBSD analysis of a secondary crack in a WT sample tested at ±0.01 strain. As is shown in Fig. 14 (a), the secondary crack was a branch from the main crack path and propagated parallel to the fusion boundary. According to the IPF&IQ map in Fig. 14 (b), the secondary crack growth occurred within a single columnar grain at approximately 50 μm from the FB. Fine sub-grain structures were observed inside the columnar grains close to the primary crack. Nevertheless, the deformation during the secondary crack propagation also leads to the formation of fine dislocation cells along the crack path. The overlaid IQ map in Fig. 14 (c) shows that a crack exists closely underneath the sample surface and propagates along the Type-II GB. In addition, the parallel low IQ lines perpendicular to the FB represent the strain localization at the solidification sub-grain boundaries. The KAM map in Fig. 14 (d) reveals the distribution of residual plastic strain induced by cyclic deformation. The misorientation distribution clearly shows the strain localization within the WM region close to the weld interface. Interestingly, little plastic strain accumulation was observed between the Type-II GB and the FB, where the hardness and composition transitions occurred [2].

3.4.3. SEM fracture surface analysis

Fig. 15 (a) and (b) show the top view and the reconstructed surface topography of a WT fracture surface. The fatigue cracks were found in the regions close to the surface, and most of the fracture was caused by ductile failure. The yellow dashed line in Fig. 15 (a) indicates the surface crack path along the FB, and the fracture surface grows further into the WM as the z-height increases. Fracture features at site 1 and site 2, indicated by the yellow arrows, were analyzed using SEM and EDS analysis. Fig. 15 (c) shows that the fracture surface at site 1 exhibits a flat crack initiation region followed by a tortuous crack growth region. As is shown in Fig. 15 (e), the crack growth was along the favorable plane but was occasionally interrupted by solidification structures. The observed feature corresponds to the stage I fracture, which exhibits fracture facets [33]. Fig. 15 (f) shows the stepwise fatigue striations and a secondary crack between the striations. The EDS analysis in Table 4 indicates the crack nucleated within the WD zone with approximately 60 % Fe content. WD ratio at the fracture surface can be estimated based on the Fe content in the BM and WM using equation [3]. The calculated weld dilutions at the crack nucleation site and the growth site are 58 % and 22 %, respectively. Hence, the dilution decreases significantly as the crack propagates into the WM region, which corresponds well to the abrupt compositional change observed in compositional profile shown in Fig. 6 (a).

Fig. 15 (d) shows the SEM image of the fracture surface at site 2. Compared with site 1, site 2 grows further into the WM and exhibits solidification features at the fracture surface. Several crack initiations were spotted close to the sample surface, and the fatigue crack growth region shows both stepwise benchmarks as well as ductile dimples. As is shown in Fig. 15 (g), the crack started with a planar, followed by the transgranular growth that forms striation marks. The intact solidification dendrites on the fracture surface indicate that the short crack growth was affected by the microstructure. The striation marks in Fig. 15 (h) indicate a continuous fatigue crack growth adjacent to the crack initiation site. Outside the fatigue region, the fracture surface shows the ductile fracture feature caused by shear stress.

4. Discussion

4.1. Weld dilution impact on local mechanical properties

Microhardness measurement is an effective approach to evaluate the materials strength and hardening due to deformation. Qiao et al. [36] showed that the hardness increase within a dissimilar weld represents the residual plastic strain accumulation that causes strain-hardening. Luo et al. [37] also adopted the hardness increases to reveal the strain hardening of WM and HAZ after ratcheting deformation. According to the chemical compositional profile in Fig. 6 (b) and the microhardness mapping in Fig. 12 (a)–(d), the increase in WM hardness coincides with the compositional change from the 1st to the 2nd WM layer, as is shown in Fig. 6 (b). Hence, the Fe content from WD might account for the low-hardness in the 1st WM layer. However, the Fe content is regarded as a solid-solution strengthening element in nickel-based alloys, and the increase of Fe content due to WD is expected to reinforce the strength and hardening of materials through interaction with dislocation motions. In addition, Delehouzee and Deruyttere [38] showed that the Fe addition has little impact on the stacking fault energy of the nickel-based alloys. Hence the contribution of stacking faults and twinning to strain hardening does not vary with the Fe content in Ni-Fe alloys. Khayat and Palmer [39] investigated the impact of Fe content on the mechanical properties of additively manufactured Alloy 625. They found that the low-Fe alloy exhibits a higher yield strength and a lower strain hardening than the high-Fe alloy. According to their result, the difference in mechanical properties is due to the grain size difference, as the low-Fe alloy possesses finer grain size than the high-Fe alloy. Little evidence from the previous literatures was found to justify the assumption that the Fe content from WD directly causes the reduction of strength and hardening of the 1st WM layer. On the other hand, the compositional effect of Fe on lowering the solubility of Nb in nickel-base alloys has been reported in previous literature [17,40]. Compared with Fe, Nb is a much stronger solid-solution strengthening element to increase the flow stress of nickel-base alloys [41,42]. As is shown in Fig. 8 (c), the high Fe content in the 1st WM layer promotes the segregation of Nb at SGBs and SSGBs, and carbon migration further increases the Nb-rich carbide formation. Therefore, the 1st WM layer exhibits a lower hardness than the 2nd WM layer due to the reduction of Nb content in the nickel-base WM matrix.

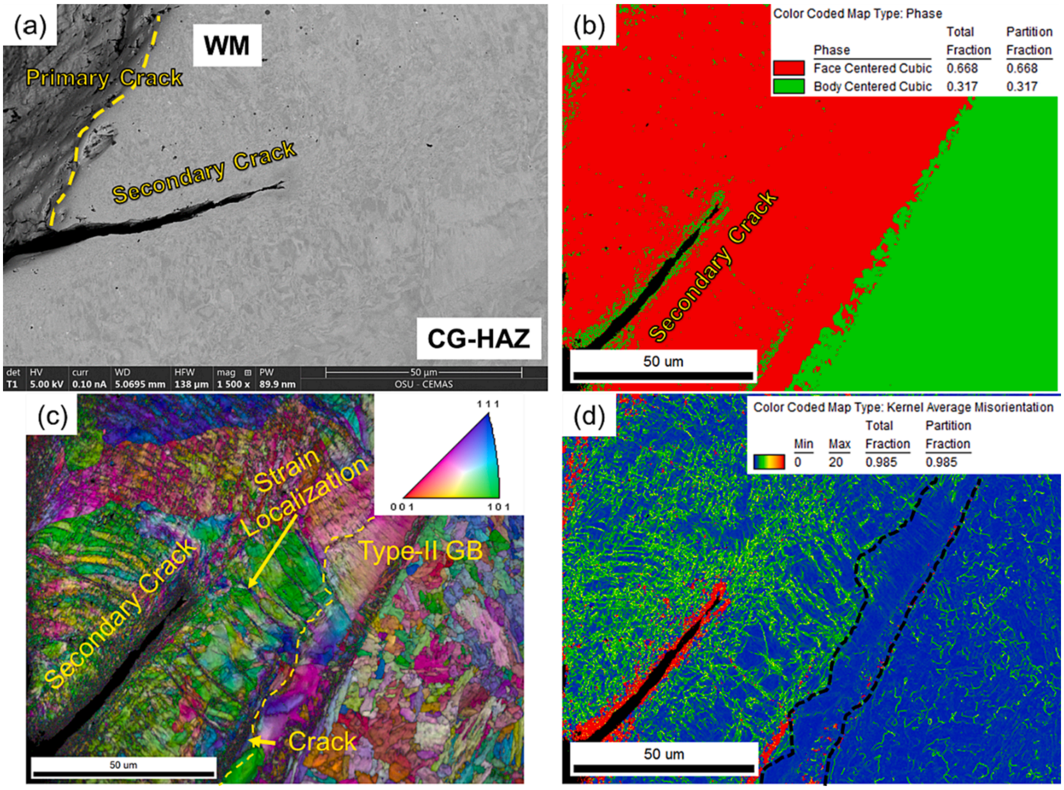

Fig. 14. EBSD analysis of the secondary crack parallel to the fusion boundary in a fatigue sample tested at ±0.01 strain. (a) SEM image of the secondary crack. (b) FCC-BCC phase distribution. (c) IPF & IQ map of the secondary crack in the vicinity of FB. (d) KAM map of the secondary crack. The BCC phases along the secondary crack are mis-indexed pixels due to low image quality along the crack. No phase transformation is expected to occur under cyclic deformation at 250 °C.

4.2. Mismatch and cyclic behavior at the weld transition

Strength and hardening mismatch affect the strain distribution within the Alloy 182-LAS dissimilar joint. The impact of hardening becomes more critical as the plastic strain significantly overweighs the elastic strain. According to Fig. 9, BM has a higher yield strength at 250 °C under uniaxial tensile loading. However, the cyclic stress responses in Fig. 10 (a), (c), (e) indicate that the Alloy 182 WM exhibits a more significant cyclic hardening tendency than the BM. On the other hand, according to the cyclic plasticity theory, kinematic hardening describes the hardening behavior, which is represented by the non-linear portions of the stress–strain curves within the plastic range [34]. The comparison between the BM and the WM stress–strain curves demonstrates that the BM exhibits less kinematic hardening than the WM. Therefore, the BM is overmatched by the WM under cyclic loading, and the mismatch increases with strain amplitudes. Compared with monotonic tensile loading, the cyclic tension–compression tests induce more sophisticated local behavior as is shown in Fig. 11 (d). At 0.01 and 0.015 strain amplitudes, the local strain variations measured by DIC become unsymmetrical and stay at a stable condition. In contrast, a significant ratchetting phenomenon occurs at the BM region at 0.02 strain amplitude, which agrees with the mismatch indicated in Fig. 10 (f). Fan et al. [35] also reported a ratcheting phenomenon within a welded joint with matching filler metal under cyclic deformation. According to their DIC results, the compressive ratcheting occurs in the IC-HAZ, while the tensile ratcheting occurred in the BM. The authors discussed that the compressive ratcheting in the IC-HAZ is caused by the compressive mean stress formed in the early cycles. However, the impact of local mismatch upon ratcheting was not taken into consideration. According to the BM behavior in Fig. 11 (d), (f), (h), the BM shifts from the asymmetrical strain variation with a compressive mean strain at ±0.01 and ±0.015 to the tensile ratcheting at ±0.02. Therefore, the increasing impact of the hardening mismatch provides a reasonable explanation for the change in BM behavior, as the stress increase within the plastic range became more evident at ±0.02 strain than at the lower strains. On the other hand, the mismatch renders a plausible explanation for the less fatigue life decrease from ±0.015 to ±0.02, as the BM endured more portion of the total strain and mitigates the cracking susceptibility at the weld interface.

Among the WT regions, the high-hardness HAZ is the only region that exhibits a fully reversed strain variation at different strain amplitudes. This indicates that the HAZ region is less affected by the local mismatch than the neighboring WM and BM regions due to its high strength. Based on the WT failure in Fig. 12 (a)–(d), the shear strain induced by mismatch is the primary cause for weld interface failure. Therefore, reducing the local mismatch between the HAZ and the WM 1st layer is beneficial to improve the resistance to LCF. The proposed strategies for improvement are tempering the HAZ hardness and reducing WD at the WM 1st layer.

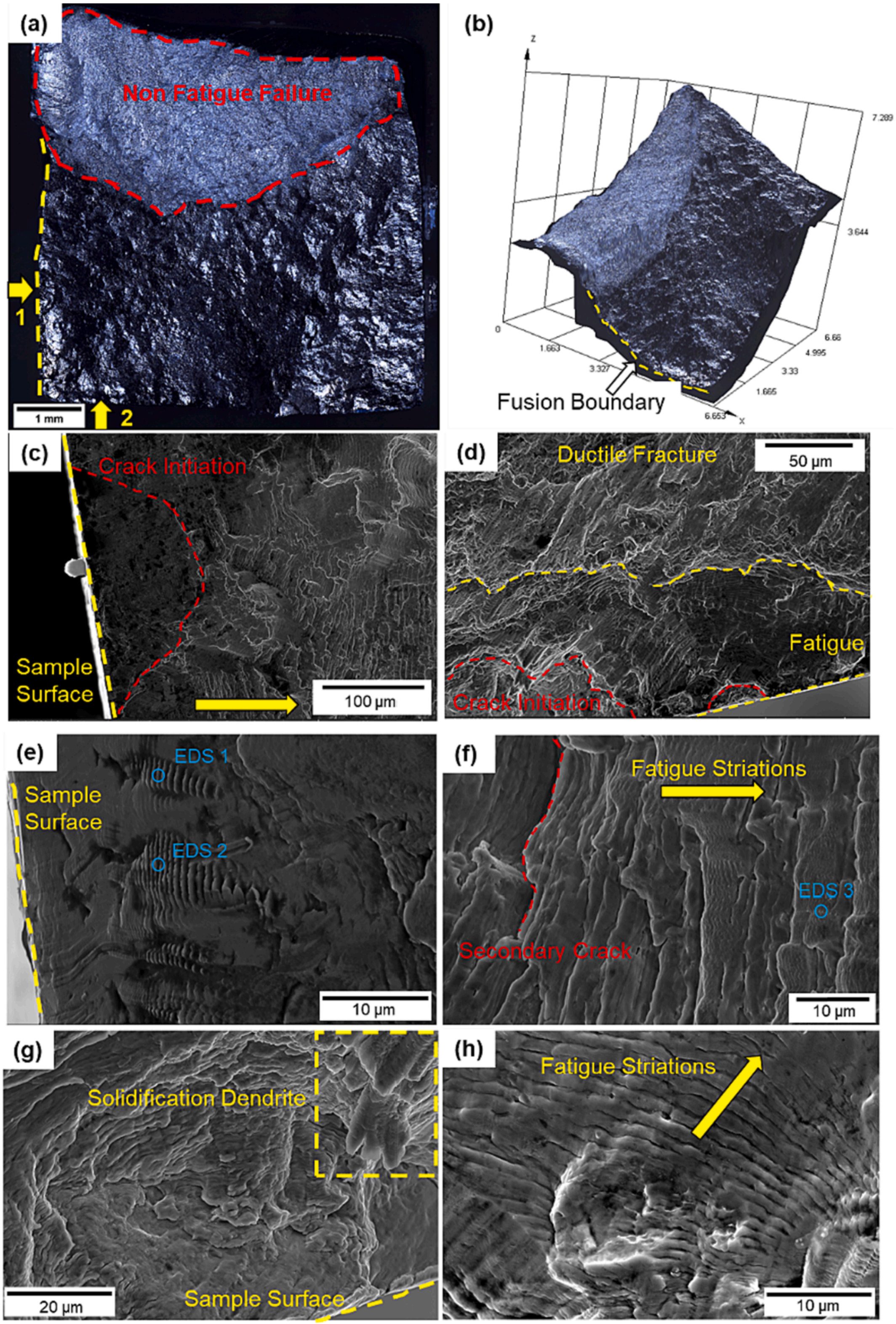

Fig. 15. OM and SEM images of the fracture surface in a WT sample tested at ±0.01 strain. (a) Top view and (b) reconstructed surface topography of the fracture surface. SEM images of crack initiations at (c) site 1 and (d) site 2. High magnification SEM images of (e) fatigue crack initiation and (f) propagation at site 1. Three EDS measurement locations were marked by the blue circles. High magnification SEM images of (g) fatigue crack initiation and (h) fatigue striations at site 2.

Table 4
Chemical composition (wt.%) of major elements measured by EDS Analysis.

	Cr	Mn	Fe	Ni
EDS 1	8.5	2.2	60.7	28.7
EDS 2	8.7	2.3	58.7	30.3
EDS 3	13.8	5.5	28.7	51.9

5. Conclusions

This paper presents a comprehensive analysis of the cyclic deformation and failure mechanism of a dissimilar joint between the Ni-based Alloy 182 and 1.25Cr-0.5Mo steel. The key finds are summarized below.

- The Alloy 182 WM undermatches the 1.25Cr-0.5Mo BM under monotonic loading but overmatches the BM under cyclic loading due to cyclic hardening.
- Strain variation within the WT regions is dominated by the local mismatch in terms of strength and hardening behavior. Both BM and WM exhibit a non-zero mean strain due to the constraining effect of the HAZ.
- The microhardness in the WM region increases with the compositional gradient from the 1st WM layer to the 2nd WM layer. The soft region adjacent to the fusion boundary is attributed to the lower solubility of Nb in the FCC matrix, which is caused by the increasing Fe content and the carbon migration due to WD.
- Fatigue crack initiation occurred in the WD region close to the interface. Dissimilar weld defects including Type II grain boundaries and solidification grain boundaries are the favorable site for strain localization and crack initiation.
- Shear strain induced by local mismatch is regarded as the primary reason for the interface failure of Alloy 182 dissimilar joint. Mitigation strategies including tempering the HAZ region and reducing WD are proposed to improve the LCF fatigue resistance.

CRediT authorship contribution statement

Shutong Zhang: Conceptualization, Methodology, Formal analysis, Visualization, Validation, Investigation. **Sebastian Romo:** Conceptualization, Methodology, Data curation, Investigation. **Rafael A. Giorjao:** Validation, Visualization, Investigation. **Kaue C. Riffel:** Investigation, Software, Visualization. **Antonio J. Ramirez:** Funding acquisition, Conceptualization, Resources, Supervision.

Declaration of Competing Interest

The authors declare that they have no known competing financial interests or personal relationships that could have appeared to influence the work reported in this paper.

Data availability

The processed data required to reproduce these findings cannot be shared at this time as the data also forms part of an ongoing study.

Acknowledgement

The project is funded by the Manufacturing and Materials Joining Innovation Center (Ma^{2}JIC), supported by the National Science Foundation Industry University Cooperative Research Center Program (IUCRC) (NSF 1539992, 1822144, and 2052747). The authors would like to appreciate the providence of advanced characterization facility from the Center for Electron Microscopy Analysis (CEMAS). The authors would also like to acknowledge the financial support from the FULBRIGHT scholarship to this program.

References

[1] C.D. Lundin, Dissimilar metal welds—transition joints literature review, Weld. J. 61 (2) (1982) 58–63.
[2] J. Hou, et al., Microstructure and mechanical property of the fusion boundary region in an Alloy 182-low alloy steel dissimilar weld joint, J. Mater. Sci. 45 (19) (2010) 5332–5338, https://doi.org/10.1007/s10853-010-4581-6.
[3] J.W. Kim, K. Lee, J.S. Kim, T.S. Byun, Local mechanical properties of Alloy 82/182 dissimilar weld joint between SA508 Gr.1a and F316 SS at RT and 320°C, J. Nucl. Mater. 384 (3) (2009) 212–221, https://doi.org/10.1016/j.jnucmat.2008.11.019.
[4] C. Jang, J. Lee, J. Sung Kim, T. Eun Jin, Mechanical property variation within Inconel 82/182 dissimilar metal weld between low alloy steel and 316 stainless steel, Int. J. Press. Vessels Pip. 85 (9) (2008) 635–646, https://doi.org/10.1016/j.ijpvp.2007.08.004.
[5] K. Fan, G.Z. Wang, F.Z. Xuan, S.T. Tu, Local fracture resistance behavior of interface regions in a dissimilar metal welded joint, Eng. Fract. Mech. 136 (2015) 279–291, https://doi.org/10.1016/j.engfracmech.2015.02.007.
[6] R. Nivas, et al., A comparative study on microstructure and mechanical properties near interface for dissimilar materials during conventional V-groove and narrow gap welding, J. Manuf. Process. 25 (2017) 274–283, https://doi.org/10.1016/j.jmapro.2016.12.004.
[7] T. Sarikka, et al., Microstructural, mechanical, and fracture mechanical characterization of SA 508-Alloy 182 dissimilar metal weld in view of mismatch state, Int. J. Press. Vessels Pip. 145 (2016) 13–22, https://doi.org/10.1016/j.ijpvp.2016.06.004.

[8] W.J. Brayshaw, A.J. Cooper, A.H. Sherry, Assessment of the micro-mechanical fracture processes within dissimilar metal welds, Eng. Fail. Anal. 97 (2019) 820–835, https://doi.org/10.1016/j.engfailanal.2019.01.048.

[9] X. Wu, J. Shuai, K. Xu, Z. Lv, Local constitutive behavior of undermatched welded joints in pipeline steel using digital image correlation technology, J. Press. Vessel Technol. 142 (5) (2020), 054502, https://doi.org/10.1115/1.4047271.

[10] S.K. Paul, S. Roy, S. Sivaprasad, H.N. Bar, S. Tarafder, Local ratcheting response in dissimilar metal weld joint: characterization through digital image correlation technique, J. Mater. Eng. Perform. 26 (10) (2017) 4953–4963, https://doi.org/10.1007/s11665-017-2919-9.

[11] Y. Zhang, J. Shuai, W. Ren, Z. Lv, Investigation of the tensile strain response of the girth weld of high-strength steel pipeline, J. Constr. Steel Res. 188 (2022), 107047, https://doi.org/10.1016/j.jcsr.2021.107047.

[12] A. Benoit, L. Rémy, A. Köster, H. Maitournam, F. Oger, Experimental investigation of the behavior and the low cycle fatigue life of a welded structure, Mater. Sci. Eng. A 595 (2014) 64–76, https://doi.org/10.1016/j.msea.2013.11.082.

[13] J.N. Dupont, C.S. Kusko, Technical note: martensite formation in austenitic/ferritic dissimilar alloy welds, Weld. J.-N. Y. 86 (2) (2007) 51.

[14] B.T. Alexandrov, J.C. Lippold, J.W. Sowards, A.T. Hope, D.R. Saltzmann, Fusion boundary microstructure evolution associated with embrittlement of Ni–base alloy overlays applied to carbon steel, Weld. World 57 (1) (2013) 39–53, https://doi.org/10.1007/s40194-012-0007-1.

[15] M.D. Rowe, T.W. Nelson, J.C. Lippold, Hydrogen-induced cracking along the fusion boundary of dissimilar metal welds, Weld. J.-N. Y. 78 (1999) pp. 31-s.

[16] H. Ming, J. Wang, E.-H. Han, Comparative study of microstructure and properties of low-alloy-steel/nickel-based-alloy interfaces in dissimilar metal weld joints prepared by different GTAW methods, Mater. Charact. 139 (2018) 186–196, https://doi.org/10.1016/j.matchar.2018.02.044.

[17] S.W. Banovic, J.N. Dupont, A.R. Marder, Dilution and microsegregation in dissimilar metal welds between super austenitic stainless steel and nickel base alloys, Sci. Technol. Weld. Join. 7 (6) (2002) 374–383, https://doi.org/10.1179/136217102225006804.

[18] D.W. Rathod, P.K. Singh, S. Pandey, S. Aravindan, Effect of buffer-layered buttering on microstructure and mechanical properties of dissimilar metal weld joints for nuclear plant application, Mater. Sci. Eng. A 666 (2016) 100–113, https://doi.org/10.1016/j.msea.2016.04.053.

[19] S.S. Sandhu, A.S. Shahi, Metallurgical, wear and fatigue performance of Inconel 625 weld claddings, J. Mater. Process. Technol. 233 (2016) 1–8, https://doi.org/10.1016/j.jmatprotec.2016.02.010.

[20] T.W. Nelson, J.C. Lippold, M.J. Mills, Nature and evolution of the fusion boundary in ferritic-austenitic dissimilar metal welds — Part 2: on-cooling transformations, Weld. J.- Weld. Res. Suppl. 10 (2000) 267–277.

[21] S.C. Yoo, K.J. Choi, C.B. Bahn, S.H. Kim, J.Y. Kim, J.H. Kim, Effects of thermal aging on the microstructure of Type-II boundaries in dissimilar metal weld joints, J. Nucl. Mater. 459 (2015) 5–12, https://doi.org/10.1016/j.jnucmat.2015.01.009.

[22] T.W. Nelson, J.C. Lippold, M.J. Mills, Investigation of boundaries and structures in dissimilar metal welds, Sci. Technol. Weld. Join. 3 (5) (1998) 249–255, https://doi.org/10.1179/stw.1998.3.5.249.

[23] J. Hou, Q. Peng, Y. Takeda, J. Kuniya, T. Shoji, Microstructure and stress corrosion cracking of the fusion boundary region in an alloy 182-A533B low alloy steel dissimilar weld joint, Corros. Sci. 52 (12) (2010) 3949–3954, https://doi.org/10.1016/j.corsci.2010.08.002.

[24] L. Dong, Q. Peng, E.-H. Han, W. Ke, L. Wang, Microstructure and intergranular stress corrosion cracking susceptibility of a SA508-52M-316L dissimilar metal weld joint in primary water, J. Mater. Sci. Technol. 34 (8) (2018) 1281–1292, https://doi.org/10.1016/j.jmst.2017.11.051.

[25] T. Nakata, H. Tanigawa, Evaluation of local deformation behavior accompanying fatigue damage in F82H welded joint specimens by using digital image correlation, Fusion Eng. Des. 87 (5–6) (2012) 589–593, https://doi.org/10.1016/j.fusengdes.2012.01.048.

[26] T. Lant, D.L. Robinson, B. Spafford, J. Storesund, Review of weld repair procedures for low alloy steels designed to minimise the risk of future cracking, Int. J. Press. Vessels Pip. 78 (11–12) (2001) 813–818, https://doi.org/10.1016/S0308-0161(01)00094-1.

[27] R. Viswanathan, D. Gandy, Weld repair of aged Cr-Mo steel piping—a review of literature, J. Press. Vessel Technol. 122 (1) (2000) 76–85, https://doi.org/10.1115/1.556154.

[28] A. Aloraier, A. Al-Mazrouee, J.W.H. Price, T. Shehata, Weld repair practices without post weld heat treatment for ferritic alloys and their consequences on residual stresses: a review, Int. J. Press. Vessels Pip. 87 (4) (2010) 127–133, https://doi.org/10.1016/j.ijpvp.2010.02.001.

[29] T. Yamamoto, K. Arii, S. Niimoto, M. Ohata, T. Tagawa, F. Minami, Investigation of bulging behavior of coke drum—a practical analysis of bulging under complex quench conditions, J. Press. Vessel Technol. 136 (6) (2014), 061401, https://doi.org/10.1115/1.4027591.

[30] J. Chen, T. Yamatomo, Z. Xia, K. Esaki, Experimental evaluation of fatgiue life of coke drum materials with weld sections, in: Proceedings of the ASME 2013 Pressure Vessels and Piping Conference, Paris, Jul. 2013.

[31] D.E. Moore, Weld repair of carbon-moly coke drums without postweld heat treatment, Bull.-Weld. Res. Counc. 412 (1996).

[32] S. Zhang, S.A. Romo, J. Penso, H. Guo, L. Ely, A.J. Ramirez, Isothermal low-cycle fatigue evaluation of external weld repair using alloy 182 filler metal with backing plate design, in: Volume 3: Design and Analysis, Virtual, Online, Aug. 2020, p. V003T03A003, doi: 10.1115/PVP2020-21574.

[33] M. Gell, G.R. Leveranti, The characteristics of stage I fatigue fracture in a high-strength nickel alloy, ACTA Metall. 16 (1968) 9.

[34] J.L. Chaboche, Time-independent constitutive theories for cyclic plasticity, Int. J. Plast. 2 (2) (1986) 149–188, https://doi.org/10.1016/0749-6419(86)90010-0.

[35] M. Fan, C. Shao, Y. Wang, X. Huo, N. Ma, F. Lu, In-situ DIC investigation on local stress-strain behavior in creep-fatigue test of dissimilar steel welded joint, Int. J. Fatigue 152 (2021), 106464, https://doi.org/10.1016/j.ijfatigue.2021.106464.

[36] D. Qiao, W. Zhang, T.-Y. Pan, P. Crooker, S. David, Z. Feng, Evaluation of residual plastic strain distribution in dissimilar metal weld by hardness mapping, Sci. Technol. Weld. Join. 18 (7) (2013) 624–630, https://doi.org/10.1179/1362171813Y.0000000144.

[37] H. Luo, G. Kang, Q. Kan, Y. Huang, Experimental investigation on the heterogeneous ratchetting of SUS301L stainless steel butt weld joint during uniaxial cyclic loading, Int. J. Fatigue 105 (2017) 169–179, https://doi.org/10.1016/j.ijfatigue.2017.08.027.

[38] L. Delehouzee, A. Deruyttere, The stacking fault density in solid solutions based on copper, silver, nickel, aluminum and lead, Acta Metall. 15 (5) (1967) 727–734.

[39] Z.R. Khayat, T.A. Palmer, Impact of iron composition on the properties of an additively manufactured solid solution strengthened nickel base alloy, Mater. Sci. Eng. A 718 (Mar. 2018) 123–134, https://doi.org/10.1016/j.msea.2018.01.112.

[40] D.W. Rathod, S. Pandey, P.K. Singh, R. Prasad, Mechanical Properties Variations and Comparative Analysis of Dissimilar Metal Pipe Welds in Pressure Vessel System of Nuclear Plants, J. Press. Vessel Technol. 138 (1) (2016) 011403, https://doi.org/10.1115/1.4031129.

[41] Y. Mishima, S. Ochiai, N. Hamao, M. Yodogawa, T. Suzuki, Solid solution hardening of nickel—role of transition metal and B-subgroup solutes, Trans. Jpn. Inst. Met. 27 (9) (1986) 656–664.

[42] A.K. Jena, M.C. Chaturvedi, The role of alloying elements in the design of nickel-base superalloys, J. Mater. Sci. 19 (10) (1984) 3121–3139, https://doi.org/10.1007/BF00549796.